# Origins of High Kinetic (*E*)-selectivity in Alkene Isomerization by a CpRu(PN) Catalyst; a Combined Experimental and Computational Approach

Thomas C. Cao, Andrew L. Cooksy, and Douglas B. Grotjahn*

Department of Chemistry and Biochemistry, 5500 Campanile Drive, San Diego State University, San Diego, CA 92182-1030

*dbgrotjahn@sdsu.edu

[Received date]

Alkene isomerization catalyst CpRu(κ$^2$-*PN*)(CH$_3$CN)]$^+$[PF$_6$]$^-$ (**Ru(acn)**) is valued for its high activity and high kinetic selectivity for forming and reacting with (*E*)-alkenes, but a mechanistic study addressing such selectivity is needed. Here, time- and temperature-dependent NMR spectroscopic studies reveal alkene complexes that were missed when lower substrate-to-catalyst ratios were used. To aid in rigorous comparison of experiment with theory, but-1-ene and isomers were used as the simplest isomerizable alkenes, and both the fast reaction of but-1-ene to form (*E*)-but-2-ene and the very slow reaction of (*Z*)-but-2-ene were performed. Temperature-dependent rate constants were obtained from fits to the time-dependent concentration profiles. The resulting Arrhenius activation energies allow comparison to a computational model. DFT calculations of the butene isomerization mechanism considered several pathways. Binding of the butene to the catalyst in an *exo* orientation is predicted to be the initial step of the preferred pathway for forming but-2-ene, with the *E* isomer favored over the *Z* by virtue of lower steric interaction while bound to the catalyst. Experimental observation of the butene-catalyst complex establishes that the rate-determining step precedes formation of the but-2-ene-catalyst complex, and DFT calculations identify breaking of the Ru-N bond with formation of a weaker agostic interaction of an allylic C-H and torsion about the Ru-P bond in a key allylic intermediate as close competitors for the rate-determining step. Experimental values for selected thermodynamic parameters of the but-1-ene isomerization were also obtained.

*Keywords: alkene, isomerization, selectivity, kinetics, DFT, ruthenium, bifunctional*

## Introduction

The isomerization of alkenes via a [3,1]-hydrogen shift is an atom economical method for the synthesis of alkenes since it requires no additional reagents other than an available isomer and the catalyst itself.[1] While many transition metal complexes can catalyze alkene isomerization reactions, few have the ability to select for the position and geometry of the double bond formed in the product.[1] For many alkene substrates, isomerization under thermodynamic control creates mixtures of products, the separation of which is difficult at best.[1] The lack of selectivity has impeded the use of isomerization as a practical method for the synthesis of olefins.

Recent developments have shown that some catalytic systems can be tuned to exhibit kinetic bias towards a particular alkene isomer.[2,3] Over a decade ago, we reported a fast alkene isomerization catalyst capable of isomerizing terminal alkenes into their internal isomers with the noteworthy attribute of doing so with unprecedented (*E*)-selectivity. CpRu complex **Ru(acn)**[1c,2a-2c] ( Figure; **Ru(acn)** = Ru$^{II}$(η$^5$-C$_5$H$_5$)(κ$^2$-PN)(CH$_3$CN)]$^+$[PF$_6$]$^-$; PN = (1-methyl-4-*tert*-butylimidazol-2-yl)-di-*iso*-propylphosphine), stands out among transition metal complexes due to its high kinetic (*E*)-selectivity and fast reactions for isomerization of many olefins, particularly unhindered chains. Typical reaction conditions for isomerization of 1-alkenes to the equilibrium ratios (at least 95:5 and for alkenes with larger substituents like phenyl, >99:1) are less than 10 minutes at 30 °C, using catalyst loadings as low as 0.05 mol%. These reaction conditions yield exclusively (*E*)-products; (*Z*)-isomers are generally not detected.

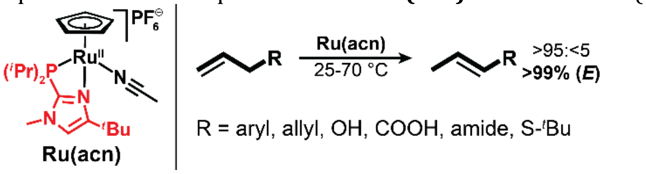

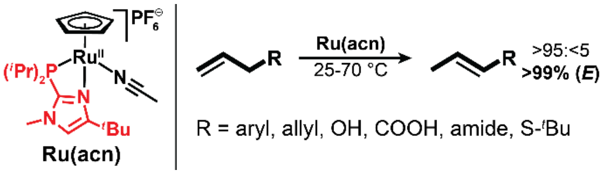

**Figure 1.** Structure of **Ru(acn)** and summary of its reactivity with terminal alkenes.

We wish to report, for the first time, a comprehensive experimental and theoretical study of butene isomerization by **Ru(acn)**, as a model for isomerizations of other 1-alkenes to (*E*)-alk-2-enes. While a previous computational study by Tao et al. described the pathway for forming (*E*)-2-pentene, the study was mostly theoretical and did not investigate the origin of the (*E*)-selectivity of **Ru(acn)**.[4] Synthetic chemists value the activity and high kinetic (*E*)-selectivity,[5] motivating us to understand both of these phenomena.

In this work, we describe the **Ru(acn)**-catalyzed isomerization of model substrate but-1-ene (**1**). New time- and temperature-dependent kinetics studies based on NMR spectroscopic data with a new set of DFT calculations of the butene mechanism were used to identify the likeliest pathway from **1** to **2*E***, the isomer (*E*)-but-2-ene, and from **1** to (*Z*)-but-2-ene **2*Z***, in order to explain the high (*E*) selectivity. The kinetics experiments have enabled us to identify previously unreported **Ru(alkene)** species.

Our computational model shows that starting from **1** and **Ru(acn)**, the initial catalyst-substrate complex **Ru(1)** discriminates against the pathway that would lead to formation of **2*Z***, suggesting a conformational justification for the strong (*E*)-selectivity.

## Experimental

**General.** Synthesis of **Ru(acn)** was undertaken as described in the literature.[2a] Reagents were purchased from Sigma-Aldrich or Acros and used as is without further purification. NMR solvents were purchased from Cambridge Isotopes and deoxygenated by bubbling nitrogen through them. Butenes were obtained from Synquest or Phillips and used without further purification. A Varian INOVA 500 MHz spectrometer was used.

**General procedure; reaction monitoring for but-1-ene.** But-1-ene stock solutions were made in a glovebox. One representative procedure is described. A Chemglass heavy-walled tube with resealable Teflon valve on the balance was charged with $C(SiMe_3)_4$ (28.4 mg, 0.0964 mmol). Any solid sticking to upper walls was rinsed down using portions of acetone-$d_6$ (total: 10.0 mL). But-1-ene was withdrawn by plastic syringe from a Schlenk flask that had been purged with the gaseous but-1-ene, and the portion of gas was slowly (over 2-3 min) injected below the surface of the acetone-$d_6$. An aliquot (900 μL) was withdrawn by syringe and added to a J. Young resealable NMR tube for analysis by $^1$H NMR spectroscopy, using 10° pulses and 10 sec delay between pulses. If the amount of but-1-ene was found to be insufficient, the contents of the J. Young NMR tube were poured back into the heavy-walled tube and more but-1-ene was added. The last aliquot tested gave the following integrations, in arbitrary units: $C(SiMe_3)_4$ set to 100.00 and but-1-ene (CH signals 98.93, 99.30, 98.60; $CH_3$ signal 298.17). We calculate 0.258 mmol in the 900 μL sample.

Catalyst stock solution was by charging a vial with **Ru(acn)** (6.2 mg, 0.0102 mmol) and adding acetone-$d_6$ (2.05 mL) for [**Ru(acn)**]$_0$ = 5.1 mM.

Each kinetics run involved adding 100 μL catalyst stock solution to 900 μL of but-1-ene stock solution. Two different kinds of NMR tubes were used: either J. Young resealable tubes, to which catalyst had to be added in the glovebox, or screw-cap NMR tubes, to which catalyst could be added at the spectrometer by injecting catalyst solution through a septum in the cap. No matter what kind of tube was used, the catalyzed reactions were so fast that only temperatures between 253 and 283 K were practical. For the J. Young experiments, the tube was placed in a stainless-steel insulated container and aluminum foil was used to cover the top of the NMR tube and container. The resulting assembly was precooled in the glovebox -30 °C freezer for at least an hour. Catalyst solution was injected quickly, and the foil-covered assembly carried to the spectrometer; typically the time between catalyst injection and placing in the probe was 3 min, and launching of the kinetics run occurred within another 2-6 min.

A second variant of the general procedure used a stock solution of but-1-ene without the internal standard. In this variant, a J. Young NMR tube on the balance was charged with an amount of $C(SiMe_3)_4$ (3-10 mg). An initial $^1$H NMR spectrum was acquired, which was analyzed to give the but-1-ene concentration. The tube was then chilled in the glovebox freezer for at least 1 h and the rest of the experiment was the same as described above.

**General procedure; reaction monitoring for (*Z*)-but-2-ene.** Catalyst stock solutions were prepared by weighing **Ru(acn)** (~12 mg) and $C(SiMe_3)_4$ (~1 mg) internal standard into a conical vial. Acetone-$d_6$ was added to the 2.0 mL graduation mark on the vial. Samples for NMR spectroscopic analysis were prepared using 1.0 mL and 0.50 mL aliquots of catalyst stock solution. In a vial, (*Z*)-but-2-ene was injected into catalyst stock solution. For the 0.50 mL aliquots, fresh acetone-$d_6$ (0.50 mL) was added to ensure adequate sample volume for NMR. Sample solution (about 0.80 mL) was added to a J. Young NMR tube with Teflon seal.

Samples were heated in a temperature-controlled oven (Robbins Scientific Flex Chem model 404) with rotating NMR tube holders. The oven was preheated to stable temperature prior to adding the NMR tube. For data acquisition, the NMR tube was removed from the oven and immediately immersed in room temperature DI water (800 mL) to cool the tube and halt reaction progress. Single $^1$H NMR spectra were acquired using a Varian 500 MHz spectrometer (8 scans, pulse angle = 30°) at 23.5 °C with a pre-acquisition delay of 60 seconds to ensure thermal equilibrium.

Initially, the kinetics experiment for **2*Z*** was performed in a more standard fashion, using NMR tubes immersed in a heated oil bath. Unfortunately, the concentration of total alkenes (as measured by integration of the $sp^2$ proton peaks relative to $C(SiMe_3)_4$ internal standard) appeared to drop over the course of the experiment. The total alkene concentration returned to initially measured values when the NMR tube was manipulated to allow mixing of the contents at the end of a run. The calculated $k$ values using this set of data gave unusually low activation barriers, which we attributed to the volatilization of **2*Z*** into the headspace of the NMR tube. This would result in lower observed concentrations of **2*Z*** relative to **2*E***, leading to faster apparent reaction rates. Hence, the rotating oven heating technique is needed.

**Computations.** Geometries for all stationary points were optimized using the B3LYP DFT method[6a,b] and a basis set combining Dunning's cc-pVDZ basis set for the main group atoms and Peterson's aug-cc-pVDZ-pp basis for the metal.[7a,b] Grimme's D2 empirical dispersion correction[8] was incorporated in view of possible interactions involving the aromatic Cp and imidazole moieties. This B3LYP-D2 methodology has been benchmarked against similar systems in previous work.[10] However, given the sensitivity of the conclusions to energy differences of 2—3 kcal/mol, single-point energy calculations were then carried out at the B3LYP-optimized geometry of each stationary point using the MN15 DFT method,[6c] a relatively large cc-pVTZ basis set[7a,b] (1432 contracted functions), and (for comparison) the COSMO and SMD solvation corrections.[9a,b] The COSMO and SMD results yielded relative free energies equal within a mean absolute deviation of 0.8 kcal mol$^{-1}$. Transition states were confirmed in all cases using vibrational analysis followed by intrinsic reaction coordinate (IRC) scans to the neighboring minimum energy structures. Natural bond order (NBO) analysis was used to model and visualize the molecular orbitals.[11] Additional details of the computational methods, as well as optimized geometries and absolute energies, are provided in the SI. All calculations were carried out using the Gaussian 09 and Gaussian 16 suites of programs[12] running on an Intel Linux cluster. Molecular visualizations were generated using CYLview 1.0565

## Results and Discussion

**Reaction intermediates.** Isomerization of **1** to **2*E*** using **Ru(acn)** was sufficiently fast that in order to get data of sufficient quality for kinetics, we used only 0.2 mol% **Ru(acn)** and temperatures well below ambient, in the range of 253 K to 283 K, using NMR spectroscopy. An example of the time-dependent concentrations of the free **1** and **2*E*** in solution is shown in Figure 2. The data are well-fitted by a Michaelis-Menten mechanism, with an effectively zeroth-order (linear) decrease in [**1**] at early times, when the reaction rate is limited by catalyst availability, and a first-order (exponential) decrease of [**1**] to the equilibrium concentration at later times. The change in reaction order occurs gradually as the concentration [**1**] drops from roughly 50 times to 20 times the catalyst concentration, meaning after 90-95% of **1** was consumed. Significantly, on closer examination, we found that it was possible to measure time-dependent concentrations at levels between ~1 and 4 × 10$^{-4}$ M of a new complex ultimately identified as **Ru(1)** in addition to **Ru(acn)** (Figure 2), which were tabulated to allow a more detailed analysis of the mechanism for comparison to the computational model.

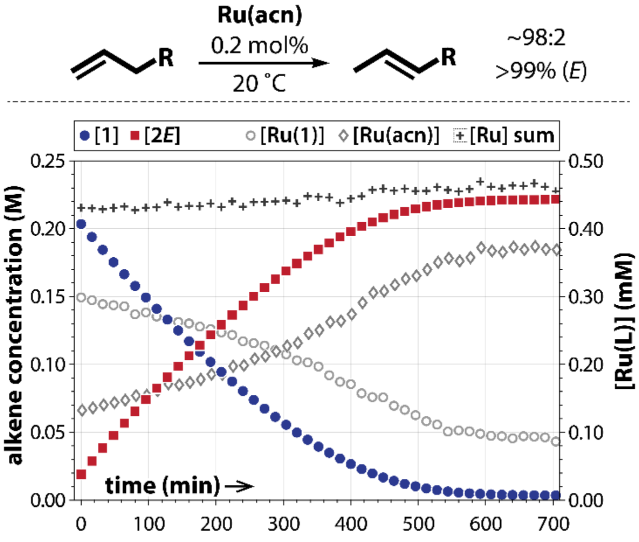

**Figure 2.** Sample concentration profiles of free alkenes but-1-ene (**1**) and (*E*)-but-2-ene (**2*E***) and observed catalyst complexes, at 253 K and with 0.2 mol% catalyst loading. [**Ru(acn)**] and [**Ru(1)**] are 1 × 10$^{-4}$ to 4 × 10$^{-4}$ M.

Alkene isomerization by **Ru(acn)** is thought to undergo a dissociative mechanism,[13] wherein loss of acetonitrile from the $18e^-$ **Ru(acn)** generates a $16e^-$ complex **Ru**[14] that can accommodate $2e^-$ donors like the π bond of an alkene (Scheme 1). Evidence for alkene complexes can be seen in the time-concentration profiles of **Ru(acn)** and **Ru(1)** during our kinetics studies. Peaks assigned to the $sp^3$ N-$CH_3$ of **Ru(1)** and **Ru(acn)** complexes could be resolved (Figure 3) and mimicked changes in the concentrations of **1** and **2*E***, respectively, in the bulk solution (Figure 2).

When the amount of **1** is maximal at the beginning of the reaction, the N-$CH_3$ signal of **Ru(acn)** at δ 3.82 is accompanied by either a signal at 3.84 (above 290 K), or at lower temperatures (e.g. 253 K), two nearly equal signals at 3.843 and 3.856 ppm, which we assign as two diastereomers of **Ru(1)**, arising from complexation of prochiral **1** to the prochiral fragment **Ru** (see also below for discussion). The intensities of the minor and major N-$CH_3$ singlets exhibit changes over time consistent with **Ru(1)** and **Ru(acn)**, respectively (**Error! Reference source not found.**). The signal for **Ru(acn)** rises gradually over time, while the signal(s) for **Ru(1)** decrease. As discussed in the SI, at 253 K, singlets ascribed to $C_5H_5$ protons at 5.10 and 5.18 ppm are also seen, and the significant

**Scheme 1.** Proposed interrelationship of observed species and postulated intermediate **Ru**

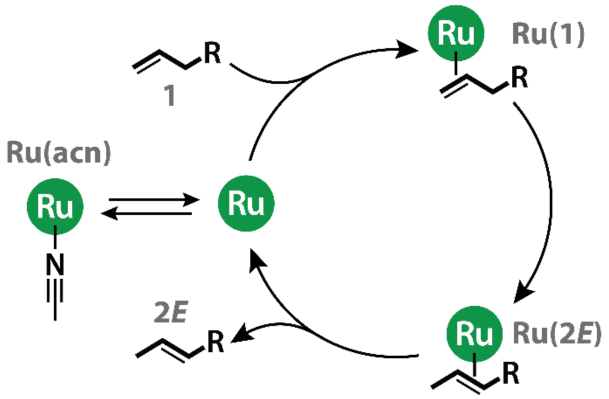

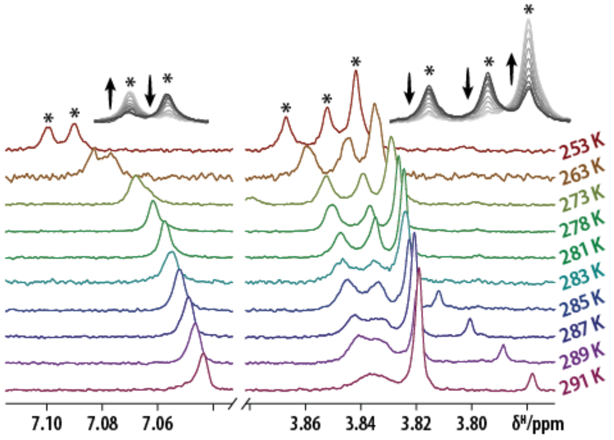

**Figure 3.** *black traces at top:* Time-dependence of assigned **Ru(acn)** and **Ru(1)** NMR signals (*). *colored traces:* Temperature dependence of N-CH$_3$ and ligand aromatic C-H signals (*) at early reaction times when amount of **1** is maximal.

downfield shift relative to 4.61 ppm for **Ru(acn)** is entirely consistent with a π-acid alkene ligand on **Ru(1)**, an assignment further supported by extensive NMR spectroscopic analysis of **Ru(ethene)** (see SI pp S2-S10).

We conclude that **Ru(acn)** exchanges with **1** to generate some **Ru(1)** prior to the first experimental measurement. As **1** is depleted by the isomerization to **2*E***, the concentration of **Ru(1)** drops, roughly in proportion. On the timescale of the experiment, therefore, **1** and **Ru(1)** are nearly in fast equilibrium. As shown in Figure 3, the two nearly equal signals at 3.843 and 3.856 ppm assigned to the two diastereomers of **Ru(1)** coalesce at higher temperatures. Lineshape analysis (see SI) and use of an Eyring plot led to the conclusion that for mutual interconversion of the two species $\Delta H^\ddagger$ = 16.0(0.6) kcal mol$^{-1}$ and .$\Delta S^\ddagger$ = 27.0(1.8) cal mol$^{-1}$ K$^{-1}$. DFT calculations find both *endo* and *exo* conformations of **Ru(1)** to have similar stabilities, as discussed below. The $\Delta H^\ddagger$ value just mentioned agrees with calculated values for creation of a 1-butene encounter complex ($\Delta H^\ddagger = 16$ kcal mol$^{-1}$), but the measured $\Delta S^\ddagger$ is significantly larger than the corresponding calculated value of 2 cal mol$^{-1}$ K$^{-1}$. Further experimental and computational study is needed to confirm the identity of the conformations involved, but we note that the experimental value appears consistent with reports in the literature. A range of experimental $\Delta S^\ddagger$ values for alkene dissociation is reported, but for simple alkenes such as those here, $\Delta S^\ddagger$ for alk-1-ene loss is greater than for ethene, and the value increases on going from propene to but-1-ene. The increase has been ascribed to greater conformational freedom of the side chain after the alk-1-ene leaves the metal,[15] and given the steric crowding of **Ru(1)** (vide infra), a relatively large $\Delta S^\ddagger$ value for dissociation of **1** seems reasonable.

After the equilibrium between **1** and **2*E*** is established (e.g., Figure 2, after 600 min), even though [**2*E***] is 500 times greater than [**Ru(acn)**]$_0$, signals belonging to a tentative **Ru(2*E*)** complex cannot be reliably identified and integrated under our conditions. Thus, it appears that **2*E*** rapidly dissociates from the catalyst and is replaced by **acn**. Our failure to observe the product-catalyst complex **Ru(2*E*)** suggests that equilibrium favors ligand dissociation of **Ru(2*E*)** much more than the equilibria for both **Ru(1)** and **Ru(acn)**, which may partly explain why **Ru(acn)** isomerizes terminal alkenes faster than internal alkenes.[16] At higher catalyst loadings, only **Ru(acn)** signals could be easily identified, consistent with competition between alkene and higher relative concentrations of **acn** outcompeting **1**/**2*E***/**2*Z*** for coordination to **Ru**.

**Reaction kinetics.** Using the time-dependent concentration data available for **1**, **2*E***, **Ru(acn)** and **Ru(1)**, rate constants were least squares fit to the time-dependent NMR spectroscopic data using a FORTRAN program *rate.f* developed and used by the Cooksy group. For any reaction mechanism entered by the user, the rate laws are numerically integrated at each time step to provide a simulated concentration profile. The program employs a 4th order Runge-Kutta integration scheme to model the kinetics and Press' numerical recipes[17] for least squares fitting and uncertainty analysis (for details see SI pages S18-S19).

**Isomerization of but-1-ene.** In these fits, we modeled the reaction step to form the complex **Ru(1)** and the step to convert **Ru(1)** to **2*E*** (Eq. 1). The forward steps are resolved by the independent measurements of the **Ru(1)** concentration. If we fit both forward reaction rate constants, a reverse reaction rate constant must also be fit to account for the non-zero equilibrium concentrations of **Ru(1)** and free **1**. It is possible to fit the data well by including a single rate constant for the overall reverse reaction **2*E*** →**1**. However, because the equilibrium concentration of **Ru(1)** then depends on forward reaction 1, this fit overestimates the value of $k_1$. Therefore, we instead fit two reverse rate constants $k_{-1}$ and $k_{-2}$:

$$\mathbf{Ru(acn)} + \mathbf{1} \underset{k_{-1}}{\overset{k_1}{\rightleftharpoons}} \mathbf{Ru(1)} \underset{k_{-2}}{\overset{k_2}{\rightleftharpoons}} \mathbf{Ru(acn)} + \mathbf{2}\boldsymbol{E}, \quad \text{(Eq. 1)}$$

where reaction 2 and reverse reaction 1 are pseudo-first order (with the **acn** concentration factored into the rate constants).

The resulting best-fit temperature-dependent rate constants given in Table 1. These rate constants were then fit to an Arrhenius rate constant expression $k = A\,e^{-E_a/RT}$, obtaining the values listed in Table 2. The activation energies

**Table 1. Fitted values of 1→2*E* rate constants. Uncertainties given are 1σ.**

| T | $k_1$ | $k_{-1}$ | $k_2$ | $k_{-2}$ |
|---|---|---|---|---|

| (K) | (L·mol-1·min-1) | (min-1) | (min-1) | (L·mol-1·min-1) |
|---|---|---|---|---|
| 253 | 37 ± 12 | 1.76 ±0.14 | 0.5 ± 1.2 | 1.3 ± 2.8 |
| 263 | 140 ± 12 | 5.51 ±0.17 | 1.6 ± 0.9 | 8.2 ± 3.8 |
| 273 | 373 ± 23 | 17.5 ±0.6 | 5.3 ± 2.9 | 25 ± 12 |
| 283 | 710 ± 140 | 48.6 ± 7.1 | 9 ± 11 | 77 ± 92 |

**Table 2. Derived 1→2*E* pre-exponential factors (*A*) and activation energies ($E_a$). Uncertainties given are 1σ.**

| step | units | ln[A/units] | $E_a$ (kcal·mol-1) |
|---|---|---|---|
| 1 | L·mol-1·min-1 | 31.7 ± 2.2 | 14.0 ± 1.2 |
| -1 | min-1 | 31.96 ± 0.34 | 15.79 ± 0.18 |
| 2 | min-1 | 28.1 ± 2.6 | 14.5 ± 1.4 |
| -2 | L·mol-1·min-1 | 38.3 ± 2.6 | 19.0 ± 1.4 |

**Table 3. Thermodynamic data for the 1→2*E* reaction.**

| **T** (K) | **K$_{eq}$** = [2*E*]$_{eq}$ / [1]$_{eq}$ | **ΔG°** (kcal·mol-1) |
|---|---|---|
| 253.1 | 61.2 ± 2.2 | -2.070 ± 0.019 |
| 263.2 | 52.1 ± 1.4 | -2.066 ± 0.014 |
| 273.1 | 42.3 ± 1.5 | -2.031 ± 0.020 |
| 283.1 | 35.4 ± 0.8 | -2.006 ± 0.014 |
|  | **ΔH°** (kcal·mol-1) | **ΔS°** (cal·K-1·mol-1) |
| This work | -2.63 ± 0.13 | -2.17 ± 0.48 |
| Gas-phase[18] | -2.99 | -3.6 |

for the forward reaction steps are relatively insensitive to the specific mechanism used to fit the rate constants, and so we have higher confidence in the $E_a$ values in Table 2 than in the individual rate constants in Table 1.

The rate constants for the reverse reactions in this study are determined by the approach to equilibrium concentrations among the reaction components at long times. In the **1**→**2*E*** reaction, equilibrium between reactant and product was sufficiently established to allow us to measure the temperature dependence of the equilibrium constant, and extract $\Delta H°$ and $\Delta S°$ values for that isomerization in acetone solvent, as given in Table 3.

The loss in entropy from **1** to **2*E*** is expected given the relative rigidity of the carbon chain when the double bond moves to the interior. Similarly, it was possible to fit enthalpy and entropy changes for the formation of the **Ru(1)** complex and **acn** from **1** + **Ru(acn)**, although the relatively low concentration of catalyst makes these values more uncertain. We determine $\Delta H° = -1.11 \pm 0.38$ kcal mol-1 and $\Delta S° = +4.1 \pm 1.4$ cal K-1 mol-1 for this complexation, indicating that the but-1-ene forms a slightly stronger bond to the ruthenium than the acetonitrile does.

The increase in entropy when the but-1-ene binds suggests that librational motions of the free acetonitrile in solution contribute more to the entropy of the system than the torsions of the butene, which are dampened upon complexation. Our calculations predict $\Delta H° = -1.23$ kcal mol-1, in excellent agreement with experiment, but the calculated $\Delta S° = -2.5$ cal K-1 mol-1, indicating that our encounter complex does not adequately model the librational dynamics of the free acetonitrile and butene in solution.

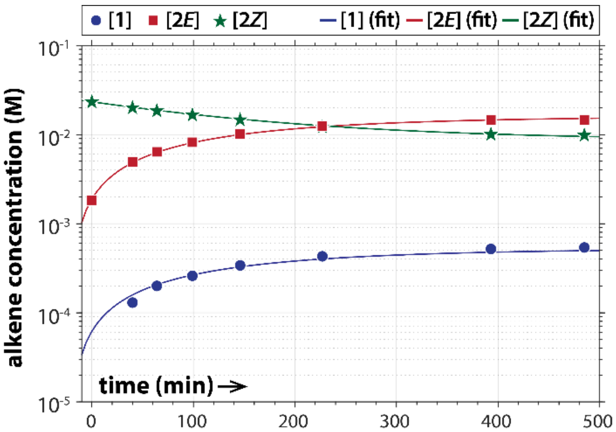

**Figure 4.** Observed and fitted concentrations for **2*Z***→ **2*E*** reaction at 343 K. Note log scale of vertical axis to better capture changes in but-1-ene concentration.

**Isomerization of (Z)-but-2-ene.** The isomerization of **2*Z*** to **2*E*** could proceed through at least three pathways: (1) catalysis of **2*Z*** to free **1**, then **1** to **2*E***; (2) catalysis of **2*Z*** to **2*E*** via **Ru(1)** without formation of free **1**; (3) direct catalysis of **2*Z*** to **2*E*** without **1** as an intermediate. For pathways (2) and (3), free **1** only appears as an isomerization from **2*E***. However, in the experiments at 319 K and 323 K, **2*E*** rapidly approaches a relative concentration of about 30 times the **1** concentration (Figure ), suggesting a rapid equilibrium between those two species on the comparatively long timescale of the consumption of **2*Z***. Furthermore, the earliest time steps in each reaction show the rise of [**2*E***] as slightly lagging the rise of [**1**], which is inconsistent with **2*E*** being formed prior to **1**. Therefore, for the purpose of determining rate constants, this reaction mechanism was modeled as

$$\mathbf{Ru(acn)} + \mathbf{2}\boldsymbol{Z} \underset{k_{-3}}{\overset{k_3}{\rightleftharpoons}} \mathbf{Ru(acn)} + \mathbf{1} \xrightarrow{k_1} \mathbf{Ru(1)} + \mathbf{acn}$$

$$\xrightarrow{k_2} \mathbf{Ru(acn)} + \mathbf{2}\boldsymbol{E};\quad \mathbf{1} \xleftarrow[k_{-4}]{} \mathbf{2}\boldsymbol{E}. \qquad \text{(Eq. 2)}$$

The rate constants were fitted to the data available at each of four temperatures. Because conditions had been adjusted to bring the reaction close to completion in reasonable times, the equilibrium between **2*E*** and **1** was reached too quickly for the rate constants associated with that step to be well-resolved, so the values of $k_1$ and $k_2$ in Eq. 2 were fixed in these fits at the values predicted by the Arrhenius parameters in Table 2. These assumptions were adequate to model the formation rate of **2*E***, but led to erroneous concentration ratios at long times. The high uncertainty in the pre-exponential factor *A* for $k_{-2}$ and the neglect of any tem-

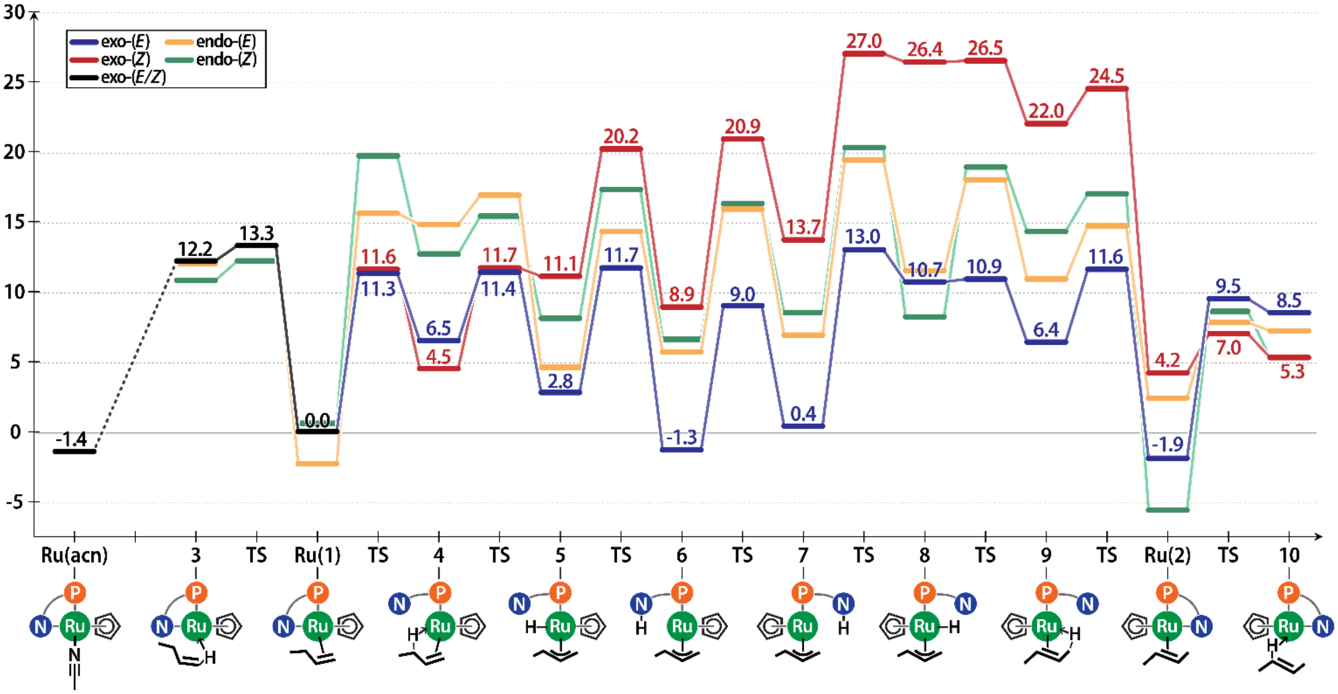

**Figure 5.** MN15/cc-pVTZ/COSMO//B3LYP/cc-pVDZ relative free energies (kcal mol$^{-1}$) of stationary points along the four pathways. Free energy values for the *exo*-(*E*) and *exo*-(*Z*) pathways are given. Some minor conformational isomerizations are omitted; figure and table with all stationary points are given in the SI. The **Ru(acn)** energy is based on relative energies of **Ru(2*E*)-acn** and **Ru(acn)-2*E*** encounter complexes.

perature dependence in *A* is sufficient to account for the discrepancy. Therefore, rather than fixing the reverse rate constants $k_{-1}$ and $k_{-2}$ in the same way, we fitted a new combined reverse rate constant $k_{-4}$ for the conversion of **2*E*** back into **1**. The values of the rate constants and the derived Arrhenius parameters appear in Tables 4 and 5. Unfortunately, even long experiment times did not bring the slow **2Z** → **2*E*** reaction close enough to equilibrium to allow a precise analysis of the thermodynamics of that reaction.

**Table 4. Fitted values of 2*Z*→2*E* rate constants. Uncertainties given are 1σ.**

| ***T*** (K) | $\boldsymbol{k_3}$ (L·mol$^{-1}$·min$^{-1}$) | $\boldsymbol{k_{-3}}$ (min$^{-1}$) | $\boldsymbol{k_{-4}}$ (min$^{-1}$) |
|---|---|---|---|
| 323.6 | 0.1470 ± 0.0016 | 2.58 ± 0.24 | (9.9 ± 1.0) × 10$^2$ |
| 333.2 | 0.467 ± 0.018 | 6.7 ± 2.0 | (2.67 ± 0.79) × 10$^3$ |
| 338.4 | 0.610 ± 0.027 | 10.5 ± 3.8 | (3.4 ± 1.1) × 10$^3$ |
| 343.2 | 0.782 ± 0.015 | 12.9 ± 1.7 | (5.21 ± 0.66) × 10$^3$ |

**Table 5. Derived 2*Z*→2*E* pre-exponential factors (*A*) and activation energies (*E*$_a$). Uncertainties given are 1σ.**

| **step** | **units** | **ln[A/units]** | ***E*$_a$ (kcal·mol$^{-1}$)** |
|---|---|---|---|
| 3 | L·mol$^{-1}$·min$^{-1}$ | 27.7 ± 4.1 | 19.0 ± 2.8 |
| -3 | L·mol$^{-1}$·min$^{-1}$ | 30.0 ± 2.5 | 18.6 ± 1.7 |
| -4 | min$^{-1}$ | 35.4 ± 2.4 | 18.3 ± 1.6 |

**Computational studies – intermediates and transition states.** DFT calculations were used to evaluate candidate catalytic cycles. Reaction pathways featuring η$^3$- as well as η$^1$-allyl intermediates were examined using DFT methods as described in SI (pp S20-S27).

The lowest energy pathways proceeded via Ru(H)(η$^3$-allyl) intermediates. Pathways with η$^1$-allyl ligands or without the hydride were examined but all of these resulted in higher energies; key details are in the SI. Four pathways via Ru(H)(η$^3$-allyl) were located (Figure 5), each associated with a stereoisomer of Ru(H)(η$^3$-allyl), varying in geometry of the allyl ligand as well as *exo*-/*endo*-coordination (Chart 1).

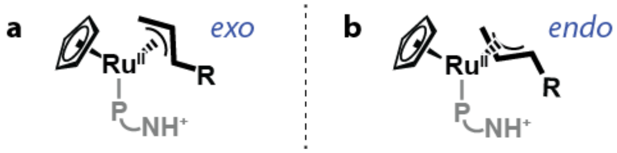

**Chart 1.** Definition of *exo* and *endo* orientations of allyl intermediates on the pathway leading to (*E*)-product.

The following discussion mentions specific intermediates in the *exo-E* pathway (Figure 5, dark blue trace) but all four pathways share similar intermediates, with two exceptions, agostic complexes **4** and **9**.

The lowest energy pathway starts with title complex **Ru(acn)** dissociating **acn** to yield five-coordinate intermediate **Ru**. The resulting vacancy is filled during the formation of the metal-alkene π-bond in **Ru(1)**. The approach of **1** to 16e$^-$ intermediate **Ru** was modeled by scanning the distance coordinate between the Ru atom of **Ru** and the terminal *sp$^2$* carbon on **1**. In this way, C1-H complex **3** was found, along with the transition state **TS**$_{\mathbf{3\text{-}Ru(1)}}$ leading to the more stable (*vide infra*) π-complex **Ru(1)**. In C-H complex **3**$^{\mathbf{exo}E}$, the coordinated C1-H distance is computed to be 1.128 Å, whereas the uncoordinated C1-H on the same terminal alkene carbon is 1.088 Å. As seen below, a more robust agostic interaction is computed to lengthen a C-H bond by more than 0.1 Å, whereas here the difference is only 0.04 Å. We therefore make use of the weakly coordinated C-H complexes **3** and **10** as proxies for free alkene plus catalytic intermediate **Ru** in order to model the dissociation of the bound alkene from the catalyst for the forward and reverse reaction along each of the four pathways. These structures have weak alkene-metal C-H bonding, but retain a unity of molecular structure that reduces the impact of basis set superposition error and cavity-separation in the solvation model.

Complex **Ru(1)** is coordinatively saturated, meaning that oxidative addition cannot occur due to lack of a vacant site to accommodate a new hydride ligand. Furthermore, the κ$^2$-PN ligand cannot act as a base when the lone pair of N is involved in bonding. Dissociation of the Ru-N bond generates a 2e$^-$ vacancy and allows the N atom to function as a base. In **TS**$_{\mathbf{Ru(1)\text{-}4}}$, the coordinative unsaturation from N dissociation is intercepted by an allylic C3-H, forming agostic complex **4**. In **4**$^{\mathbf{exo}E}$, the agostic C3-H bond distance is computed to be 1.222 Å, whereas the uncoordinated C3-H on the same carbon is 1.095 Å. Moreover the distances between Ru and alkene sp$^2$ carbons are distorted: C1-Ru is 2.227 Å, whereas C2-Ru is shortened to 2.110 Å to accommodate the neighboring agostic interaction at C3. Next, oxidative addition of the agostic C3-H bond to **Ru** gives hydride intermediate **5**, and subsequently the κ$^1$-P ligand then reductively deprotonates the hydride to give the η$^3$-allyl complex **6**. Comparing allyl complexes **5**$^{\mathbf{exo}E}$ and **6**$^{\mathbf{exo}E}$, reductive deprotonation is calculated to change the C3-Ru distance the most of all, likely because the hydride ligand in **5**$^{\mathbf{exo}E}$ is closest to C3: changes in the C1-Ru, C2-Ru, and C3-Ru distances are -0.004, -0.030 and -0.037 Å, respectively.

Conformational change of **6** is needed, since the road to **Ru(2*E*)** requires the NH hydrogen on the PN ligand, which originated from C3 of **1**, to reach C1 Torsion of the Cp-Ru-allyl moiety occurs along the Ru-P bond axis, where the allyl ligand migrates to a sterically similar environment on the opposing enantioface of **Ru**, resulting in **7**. Although the step from **6** to **7** is only a conformational change, for three of the four pathways shown in Figure 5 this step is associated with a barrier of 7-8 kcal mol$^{-1}$, which apparently arises from an increasing number of H-H steric interactions. For example, **6**$^{\mathbf{exo}E}$ has 12 such interactions involving H-H distances <2.3 Å while **7**$^{\mathbf{exo}E}$ has 16.

Oxidative protonation of Ru by the N-H bond in **TS**$_{\mathbf{7\text{-}8}}$ yields Ru$^{\mathrm{IV}}$ hydride intermediate **8**. Reductive elimination of Ru(H) in **TS**$_{\mathbf{8\text{-}9}}$ to the allyl forms agostic complex **9**. Complex **9**$^{\mathbf{exo}E}$ is computed to have structural features similar to those of **4**$^{\mathbf{exo}E}$: the agostic C1-H bond distance is computed to be 1.210 Å, whereas the two uncoordinated C1-H distances are 1.097 and 1.098 Å. Moreover the distances between Ru and alkene sp$^2$ carbons are distorted: C3-Ru is 2.268 Å, whereas C2-Ru is shortened to 2.122 Å to accommodate the neighboring agostic interaction at C1. The Ru-alkene and Ru-CH distances in **9**$^{\mathbf{exo}E}$ are all larger by 0.02-0.04 Å than for **4**$^{\mathbf{exo}E}$, consistent with the greater steric demands of **2*E*** compared with those of **1**. Dissociation of the agostic CH in **TS**$_{\mathbf{9\text{-}Ru(2E)}}$ gives π-complex **Ru(2*E*)**. The Ru-alkene distances in **Ru(2*E*)**$^{\mathbf{exo}E}$ are 2.233 and 2.252 Å, greater than **Ru(1)**$^{\mathbf{exo}E}$ (2.209 and 2.228 Å), consistent with greater steric demand in the **2*E*** complex. In **TS**$_{\mathbf{Ru(2\mathit{E})\text{-}10}}$, the **2*E*** ligand migrates to yield unstable C-H complex **10**. Once again, the greater steric demands around the coordinated internal alkene C-H in **10**$^{\mathbf{exo}E}$ lead to longer metal-ligand distances: Ru-C 2.689 vs 2.461 Å in **3**$^{\mathbf{exo}E}$, and Ru-H 2.001 vs. 1.969 Å in **3**$^{\mathbf{exo}E}$.

Tao et al. described the *exo*-(*E*) pathway for transformation of 1-pentene to (*E*)-2-pentene.[4] We examine four competing pathways for butene. Our *exo*-(*E*) calculations generally reproduce theirs, but with additional smaller conformational changes with low barriers. In general, their computed bond distances for various metal-alkene interactions tend to be greater than ours, but by less than 0.08 Å, which is not chemically significant and expected given the differences in basis set and treatment of dispersion.

**Why the (*E*)-selectivity?** Four pathways were characterized, that differ in relative stereochemistry between prochiral alkene and prochiral metal fragment Ru (Figure 5). Ultimately, we conclude that the lowest energy pathway is *exo*-(*E*), but first let us look at the others. Both *endo* pathways start with the *endo*-coordinated diastereomer of **Ru(1)** and are clearly less favorable for formation of but-2-ene than the corresponding *exo* pathways, given the significantly higher barriers encountered at **TS**$_{\mathbf{Ru(1)\text{-}4}}$. Figure 6 shows the greater interaction between alkene and catalyst alkyl groups in **TS**$_{\mathbf{Ru(1)\text{-}4}}^{\mathbf{endo}E}$ that accounts for the 5—6 kcal mol$^{-1}$ higher activation energy at this early stage of the *endo* pathway. The reaction diagrams in Figure 5 are similar for the *endo*-(*E*) and *endo*-(*Z*) pathways, both in terms of individual barriers and the free energies of the intermediates.

In contrast, from *exo*-coordinated **1**, the *exo*-(*Z*)-pathway begins to rise in energy ~10 kcal mol$^{-1}$ above the *exo*-(*E*) pathway at **5** and **TS**$_{\mathbf{5\text{-}6}}$, and remains so over several steps, rising further to ~15 kcal mol$^{-1}$ between **TS**$_{\mathbf{7\text{-}8}}$ and **TS**$_{\mathbf{9\text{-}Ru(2x)}}$ (x = *E* or *Z*). The individual barriers for the *exo*-(*Z*) pathway are not vastly greater than for *exo*-(*E*), but the free energies of the (*E*)- and (*Z*)-intermediates and TS remain separated by ~10-15 kcal/mol from **5** all the way to **TS**$_{\mathbf{9\text{-}Ru(2x)}}$. A likely explanation is restriction of conformational freedom about the Ru center, due to inner-sphere crowding resulting from the oxidation of Ru$^{\mathrm{II}}$ to Ru$^{\mathrm{IV}}$ as well as the need to accommodate an additional hydride ligand. These changes force the substrate to interact more strongly with steric bulk of the PN ligand, illustrated for intermediate **6** in Figure 7. More specifically, the energy increase along the *Z* pathway is due in part to the axial interaction between the isopropyl groups of the PN ligand and the methyl substituent on the allyl ligand. In addition, the lower part of Figure 7 looks more broadly at noncovalent H---H interactions with internuclear distances less than 2.2 Å: **6**$^{\mathbf{exo}E}$ has 6 whereas **6**$^{\mathbf{exo}Z}$ has 10.

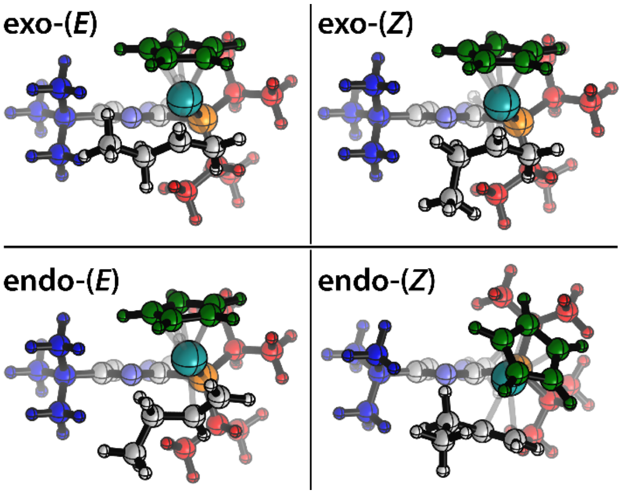

**Figure 6.** B3LYP-D2/cc-pVDZ optimized geometries of alkene in relation to metal center for $\mathbf{TS_{Ru(1)-4}}$ at the (top left) *exo*-(*E*), (top right) *exo*-(*Z*), (bottom left) *endo*-(*E*), and (bottom right) *endo*-(*Z*) geometries.

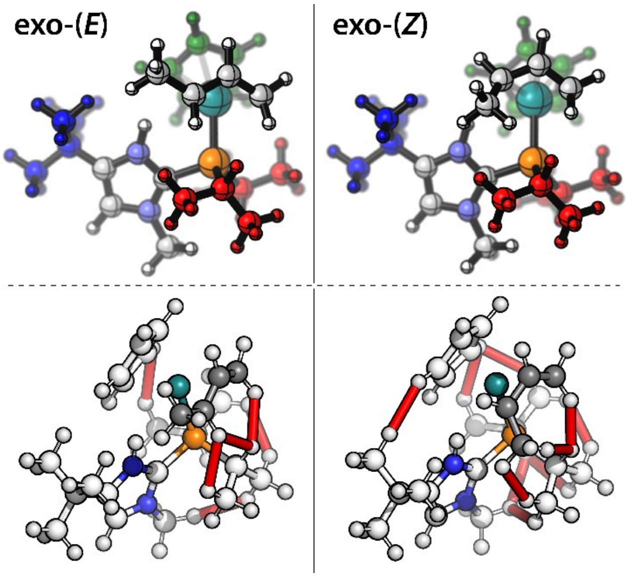

**Figure 7.** Upper: B3LYP-D2/cc-pVDZ optimized geometries of (left) $\mathbf{6}^{exoE}$ and (right) $\mathbf{6}^{exoZ}$, showing the interaction with *i*-Pr with the methyl group of the allyl ligand. Lower: alternative views of the same structures, with the noncovalent H---H interactions with internuclear distances less than 2.2 Å highlighted by red lines.

Selection of either (*E*)- or (*Z*)-pathways occurs at $\mathbf{TS_{Ru(1)-4}}$. Dissociation of the ligand nitrogen forms a 16e$^-$ Ru center and allows an agostic interaction with either of two diastereotopic C3-H of coordinated **1**. The choice of which C3-H agostic interaction conformationally locks the bound alkene **1** to adopt either pro-(*E*)- or pro-(*Z*)- geometries.

Although individual forward reaction steps for the *exo*-(*Z*) pathway appear surmountable, the *exo*-(*E*) pathway is uniformly more favorable. Correspondingly low barriers for the reverse reaction steps of the *exo*-(*Z*) pathway also contribute to strong kinetic bias towards the **1**→**2*E*** over the **1**→**2*Z*** reaction. Therefore, the computational model reproduces the experimentally observed (*E*)-selectivity.

**Rate-determining steps and energetic span.** A key finding is that the steepest free energy activation barriers $G_a$ in the calculated *exo*-(*E*) reaction diagram occur at the first step after the alkene π complex, during which the Ru-N bond breaks and a weaker C-H agostic interaction forms ($\mathbf{TS_{Ru(1)-4}}$ $G_a$ =11.3 kcal mol$^{-1}$), at the Ru-P torsion ($\mathbf{TS_{6-7}}$, 10.3 kcal mol$^{-1}$), and at the but-2-ene dissociation ($\mathbf{TS_{Ru(2\mathit{E})-10}}$, 11.4 kcal mol$^{-1}$), making these the likeliest candidates for the rate-determining step (RDS) of the **1**→**2*E*** reaction. The experimental data unambiguously indicate that the RDS occurs at some point after formation of **Ru(1)** and *before* formation of **Ru(2*E*)**, because no other catalyst-derived complex (catalyst-alkene or catalyst-allyl) builds up a comparable concentration to that of **Ru(1)**. The absence of other identifiable species rules out **Ru**(**2*E***) → **10** as the RDS. As shown in Figure 2, at any given time during the reaction, the sum [**Ru(acn)**]+[**Ru(1)**] is roughly constant and accounts for nearly all of the catalyst present. The calculations indicate that the correct RDS occurs at **Ru**(**1**) → **4**, although **6** → **7** remains a viable candidate. The assignment of the RDS to the breaking of the Ru-N bond and formation of the allylic C-H agostic interaction is consistent with the findings of Tao et al., who found a free energy barrier of 11 kcal mol$^{-1}$ for the same step in the pentene reaction.[4]

The calculated $G_a$ values combine both the Arrhenius activation energy $E_a$ and the entropic contribution to the Arrhenius pre-exponential factor, and therefore should be good indicators of the RDS, the step with the slowest reaction rate. However, only the activation energy $E_a$ (not $G_a$) carries the temperature dependence on which the experimental activation barriers in Tables 2 and 5 are based. For example, we should compare the $E_a$ value in Table 2 derived from $k_2$ (14.5 kcal/mol) to the calculated $E_a$ at $\mathbf{TS_{Ru(1)-4}}$ of 14.0 kcal/mol, which falls well within the expected error for DFT calculations on systems of this type.[19]

The energetic span of the reaction offers a more accurate relationship between the calculated mechanism and the relative efficiencies of competing catalytic pathways.[20a,b] The free energies in Figure 5 and Eq. 2 in Kozuch[20b] predict turnover frequencies of 7.75 min$^{-1}$ for the exo-(*E*) pathway and less than 10$^{-3}$ min$^{-1}$ for the other three pathways, indicating that the exo-(*E*) pathway is indeed the most effective by 3-4 orders of magnitude.

Although the *exo*-(*E*) pathway appears most favorable for the **1**→**2*E*** reaction, the reaction **2*Z***→**1,** which was also carried out in this work, appears to have similarly favorable free energy profiles following either the *endo*-(*Z*) or *exo*-(*Z*) pathways (from right to left in Figure 5). The RDS for both pathways appears at $\mathbf{TS_{9-Ru(2x)}}$ (x = *E* or *Z*), which presents energy barriers $G_a$ and $E_a$ of 20-22 kcal mol$^{-1}$, comparable to the value of 19 kcal mol$^{-1}$ for the forward energy barrier in Table 5.

## Conclusions

This detailed experimental and computational study of the catalysis of **1** to **2*E*** and **2*Z*** by catalyst **Ru(acn)** finds that the observed high *E* selectivity likely arises from increased steric interaction in the (*Z*)-forming intermediates, exemplified by the allyl species **6**. Experimental observation of the **Ru(1)** complex establishes that the rate-determining step occurs prior to formation of the 2-alkene on the catalyst, and computations suggest that the RDS is the initial breaking of the Ru-N bond in Ru(1) with formation of a weaker agostic interaction with one allylic C-H bond and the metal. Temperature-dependent measurements have determined activation barriers in good agreement with calculations.

## SUPPORTING INFORMATION

Characterization of alkene complexes, details regarding kinetics analysis and computations, optimized geometries and discussion of one alternate pathway (PDF).

## Acknowledgements

Funding for this work was provided by NSF grant CHE-1800598, with equipment support for the computational work provided by NSF CHE-0947087 and DoD W911NF-10-1-0157. We thank Erik R. Paulson and Raphael Tavares de Sa, who provided early data for this project and helpful discussions.

## References

1. (a) Crabtree, R. H. *The Organometallic Chemistry of the Transition Metals*, 7th edition (John Wiley & Sons, 2019. (b) Hassam, M.; Taher, A.; Arnott, G. E.; Green, I. R.; van Otterlo, W. A. L., Isomerization of allylbenzenes. *Chem. Rev. (Washington, DC, US)* **2015**, *115*, 5462-5569. (c) Grotjahn, D. B.; Larsen, C. R.; Erdogan, G., Bifunctional Catalyst Control of Alkene Isomerization. *Top. Catal.* **2014**, *57*, 1483-1489. (d) Molloy, J. J.; Morack, T.; Gilmour, R., Positional and Geometrical Isomerisation of Alkenes: The Pinnacle of Atom Economy. *Angew. Chem. Int. Ed.* **2019**, *58*, 13654-13664.

2. (*E*)-selectivity: (a) Grotjahn, D. B.; Larsen, C. R.; Gustafson, J. L.; Nair, R; Sharma, A., Extensive isomerization of alkenes using a bifunctional catalyst: an alkene zipper. *J. Am. Chem. Soc.* **2007**, *129*, 9592–9593. (b) Erdogan, G.; Grotjahn, D. B., Mild and selective deuteration and isomerization of alkenes by a bifunctional catalyst and deuterium oxide. *J. Am. Chem. Soc.* **2009**, *131*, 10354–10355. (c) Larsen, C. R; Grotjahn, D. B., Stereoselective alkene isomerization over one position. *J. Am. Chem. Soc.* **2012**, *134*, 10357–10360. (d) Paulson, E. R.; Moore, C. E.; Pullman, D. P.; Sindewald, R. W.; Cooksy, A. L.; Rheingold, A. L.; Grotjahn, D. B., Dynamic π-Bonding of Imidazolyl Substituent in a Formally 16-electron Cp*Ru($\kappa^2$-*P*,*N*)$^+$ Catalyst Allows Dramatic Rate Increases in (*E*)-Selective Monoisomerization of Alkenes. *ACS Catal.* **2019**, *9*, 7217-7231. (e) Wang, Y.; Qin, C.; Jia, X.; Leng, X.; Huang, Z., An Agostic Iridium Pincer Complex as a Highly Efficient and Selective Catalyst for Monoisomerization of 1-Alkenes to trans-2-Alkenes. *Angew. Chem., Int. Ed.* **2017**, *56*, 1614-1618.

3. (*Z*)-selectivity: (a) Chen, C.; Dugan, T. R.; Brennessel, W. W.; Weix, D. J.; Holland, P. L., *Z*-selective alkene isomerization by high-spin cobalt(II) complexes. *J. Am. Chem. Soc.* **2014**, *136*, 945–955. (b) Becica, J.; Glaze, O. D.; Wozniak, D. I.; Dobereiner, G. E., Selective Isomerization of Terminal Alkenes to (*Z*)-2-Alkenes Catalyzed by an Air-Stable Molybdenum(0) Complex. *Organometallics* **2018**, *37*, 482-490. (c) Weber, F.; Schmidt, A.; Roese, P.; Fischer, M.; Burghaus, O.; Hilt, G., Double-Bond Isomerization: Highly Reactive Nickel Catalyst Applied in the Synthesis of the Pheromone (9*Z*,12*Z*)-Tetradeca-9,12-dienyl Acetate. *Org. Lett.* **2015**, *17*, 2952-2955. (d) Schmidt, A.; Noedling, A. R.; Hilt, G., An Alternative Mechanism for the Cobalt-Catalyzed Isomerization of Terminal Alkenes to (*Z*)-2-Alkenes. *Angew. Chem. Int. Ed.* **2015**, *54*, 801-804.

4. Tao, J.,; Sun, F.; Fang, T., Mechanism of alkene isomerization by bifunctional ruthenium catalyst: a theoretical study. *J. Organomet. Chem.* **2012**, *698*, 1–6.

5. (a) Miura, T.; Nakahashi, J.; Sasatsu, T.; Murakami, M., Synthesis of γ-Boryl-Substituted Homoallylic Alcohols with anti Stereochemistry Based on a Double-Bond Transposition. *Angew. Chem. Int. Ed.* **2019**, *58*, 1138-1142. (b) Sytniczuk, A.; Forcher, G.; Grotjahn, D. B.; Grela, K., Sequential alkene isomerization and ring-closing metathesis in production of macrocyclic musks from biomass. *Chem. Eur. J.* **2018**, *24*, 10403-10408. (c) Liniger, M.; Liu, Y.; Stoltz, B. M., Sequential ruthenium catalysis for olefin isomerization and oxidation: Application to the synthesis of unusual amino acids. *J. Am. Chem. Soc.* **2017**, *139*, 13944-13949. (d) Higman, C. S.; de Araujo, M. P.; Fogg, D. E., Tandem catalysis versus one-pot catalysis: ensuring process orthogonality in the transformation of essential-oil phenylpropenoids into high-value products via olefin isomerization-metathesis. *Catal. Sci. Technol.* **2016**, *6*, 2077-2084. (e) Schrock, R. R.; Grotjahn, D. B.; Erdogan, G.; Larsen, C. R.; Dobereiner, G. E.. A One-Pot Tandem Olefin Isomerization/Metathesis-Coupling (ISOMET) Reaction. *ACS Catal.* **2014**, *4*, 3069–3076. (f) Curto, J. M.; Dickstein, J. S.; Berritt, S.; Kozlowski, M. C., Asymmetric Synthesis of α-Allyl-α-Aryl α-Amino Acids by Tandem Alkylation/π-Allylation of α-Iminoesters. *Org. Lett.* **2014**, *16*, 1948-1951.

6. (a) Becke, A. D., Density-functional thermochemistry. III. The role of exact exchange. *J. Chem. Phys.* **1993**, *98*, 5648-5652. (b) Lee, C.; Yang, W.; Parr, R. G.. Development of the Colle-Salvetti correlation-energy formula into a functional of the electron density. *Phys. Rev. B* **1988**, *37*, 785-789. (c) Yu, H. S.; He, X.; Li, S. L.; D. G. Truhlar, MN15: A Kohn-Sham Global-Hybrid Exchange-Correlation Density Functional with Broad Accuracy for Multi-Reference and Single-Reference Systems and Noncovalent Interactions, *Chem. Sci.* **2016**, *7*, 5032-5051.

7. (a) Dunning Jr., T. H., Gaussian basis sets for use in correlated molecular calculations. I. The atoms boron through neon and hydrogen. *J. Chem. Phys.* **1989**, *90*, 1007-1023. (b) Peterson, K. A.; Puzzarini, C., Systematically convergent basis sets for transition metals. II. Pseudopotential-based correlation consistent basis sets for the group 11 (Cu, Ag, Au) and 12 (Zn, Cd, Hg) elements. *Theor. Chem. Acc.* **2005**, *114*, 283-296.

8. Grimme, S., Semiempirical GGA-type density functional constructed with a long-range dispersion correction. *J. Computational Chem*. **2006**, *27*, 1787–1799.

9. (a) Barone, V.; Cossi, M., Quantum Calculation of Molecular Energies and Energy Gradients in Solution by a Conductor Solvent Model. *J. Chem. Phys. A* **1998**, *102*, 1995-2001. (b) Marenich, A. V.; Cramer, C. J.; Truhlar, D. G., Universal Solvation Model Based on Solute Electron Density and on a Continuum Model of the Solvent Defined by the Bulk Dielectric Constant and Atomic Surface Tensions. *J. Phys. Chem. B* **2009**, *113*, 6378–6396.

10. Frisch, M. J.; Trucks, G. W.; Schlegel, H. B.; Scuseria, G. E.; Robb, M. A.; Cheeseman, J. R.; Scalmani, G.; Barone, V.; Petersson, G. A.; Nakatsuji, H.; Li, X.; Caricato, M.; Marenich, A. V.; Bloino, J.; Janesko, B. G.; Gomperts, R.; Mennucci, B.; Hratchian, H. P.; Ortiz, J. V.; Izmaylov, A. F.; Sonnenberg, J. L.; Williams-Young, D.; Ding, F.; Lipparini, F.; Egidi, F.; Goings, J.; Peng, B.; Petrone, A.; Henderson, T.; Ranasinghe, D.; Zakrzewski, V. G.; Gao, J.; Rega, N.; Zheng, G.; Liang, W.; Hada, M.; Ehara, M.; Toyota, K.; Fukuda, R.; Hasegawa, J.; Ishida, M.; Nakajima, T.; Honda, Y.; Kitao, O.; Nakai, H.; Vreven, T.; Throssell, K.; Montgomery, J. A., Jr.; Peralta, J. E.; Ogliaro, F.; Bearpark, M. J.; Heyd, J. J.; Brothers, E. N.; Kudin, K. N.; Staroverov, V. N.; Keith, T. A.; Kobayashi, R.; Normand, J.; Raghavachari, K.; Rendell, A. P.; Burant, J. C.; Iyengar, S. S.; Tomasi, J.; Cossi, M.; Millam, J. M.; Klene, M.; Adamo, C.; Cammi, R.; Ochterski, J. W.; Martin, R. L.; Morokuma, K.; Farkas, O.; Foresman, J. B.; Fox, D. J., Gaussian 16, Revision B.01; Gaussian, Inc.: Wallingford CT, 2016.

11. (a) Arita, A. J.; Cantada, J.; Grotjahn, D. B.; Cooksy, A. L., Computational Study of the Extensive Role of Heterocyclic Ligands in Acetylene Hydration by a Bifunctional Organometallic Catalyst. *Organometallics* **2013**, *32*, 6867–6870. (b) Grotjahn, D. B.; Zeng, X.; Cooksy, A. L., Alkyne-to-Vinylidene Transformation on Trans-(Cl)Rh(Phosphine)$_2$: Acceleration by a Heterocyclic Ligand and Absence of Bimolecular Mechanism. *J. Am. Chem. Soc.* **2006**, *128*, 2798–2799.

12. Foster, J. P.; Weinhold, F., Natural Hybrid Orbitals. *J. Am. Chem. Soc.* **1980**, *102*, 7211–7218.

13. Acetonitrile exchange on CpRu(acn)$_3^+$ is dissociative: Luginbuehl, W; Zbinden, P.; Pittet, P. A.; Armbruster, T.; Buergi, H. B.; Merbach, A. E.; Ludi, A., Structure and reactivity of ruthenium half-sandwich compounds: crystal and molecular structure and acetonitrile exchange kinetics and mechanism of tris(acetonitrile)($\eta^6$-benzene)ruthenium(2+) and tris(acetonitrile)($\eta^5$-cyclopentadienyl)ruthenium(+), *Inorg. Chem.* **1991**, *30*, 2350-2355.

14. (a) For the isolable Cp* analog of **Ru**, characterized by X-ray diffraction, see reference 2(d).

15. (a) Hirsekorn, K. F.; Hulley, E. B.; Wolczanski, P. T.; Cundari, T. R., Olefin substitution in (silox)$_3$M(olefin) (silox = tBu$_3$SiO; M = Nb, Ta): The role of density of states in second vs third row transition metal reactivity, *J. Am. Chem. Soc.* **2008**, *130*, 1183-1196. (b) Huber, B. J.; Poe, A. J., Substitution kinetics of some tetracarbonyl(η$^2$-alkene)osmium complexes, *Inorg. Chim. Acta* **1994**, *227*, 215-221. (c) Angelici, R. J.; Loewen, W., Kinetic studies of olefin replacement in cyclopentadienylmanganese-olefin-dicarbonyl complexes, *Inorg. Chem.* **1967**, *6*, 682-686.

16. (a) Concomitant to these studies we made similar conclusions in ref. 2(d). There we cited literature examples of the preference of selected metal complexes for less hindered alkenes, e.g. for 1-alkenes over their 2-alkene isomers.

17. Press, W. H., *Chemical Recipes in Fortran*. 2 ed.; Cambridge University Press: Cambridge, U.K., 1992.

18. (a) Meyer, E. F.; Stroz, D. G., Thermodynamics of n-Butene Isomerization, *J Am. Chem. Soc.* **1972**, *94* 6344-6347. (b) Prosen, E. J.; Maron, F. W.; Rossini, F. D., Heats of combustion, formation, and isomerization of ten C4 hydrocarbons, *J. Res. NBS*, **1951**, *46*, 106-112.

19. Zhao, Y.; Truhlar, D. G., Density Functional Calculations of E2 and S$_N$2 Reactions: Effects of the Choice of Density Functional, Basis Set, and Self-Consistent Iterations. *J. Chem. Theory & Comput.* **2010**, *6*, 1104-1108.

20. (a) Kozuch, S.; Shaik, S., How to Conceptualize Catalytic Cycles? The Energetic Span Model. *Acc. Chem. Res.* **2011**, *44*, 101-110. (b) Kozuch, S. A., refinement of everyday thinking: the energetic span model for kinetic assessment of catalytic cycles. *WIREs Comput. Molec. Sci.* **2012**, *2*, 795-815.

# Table of contents graphic